

Missing stellar mass in SED fitting: spatially unresolved photometry can underestimate galaxy masses

R. Sorba[★] and M. Sawicki[★]

Department of Astronomy and Physics and the Institute for Computational Astrophysics, Saint Mary's University, 923 Robie Street, Halifax, Nova Scotia, B3H 3C3, Canada

Accepted 2015 May 27. Received 2015 May 8; in original form 2014 November 2

ABSTRACT

We fit model spectral energy distributions (SEDs) to each pixel in 67 nearby ($\langle z \rangle = 0.0057$) galaxies using broad-band photometry from the Sloan Digital Sky Survey and *GALEX*. For each galaxy, we compare the stellar mass derived by summing the mass of each pixel to that found from fitting the entire galaxy treated as an unresolved point source. We find that, while the pixel-by-pixel and unresolved masses of galaxies with low specific star formation rates (sSFRs, such as ellipticals and lenticulars) are in rough agreement, the unresolved mass estimate for star-forming galaxies is systematically lower than the measurement from spatially resolved photometry. The discrepancy is strongly correlated with sSFR, with the highest sSFRs in our sample having masses underestimated by 25 per cent (0.12 dex) when treated as point sources. We found a simple relation to statistically correct mass estimates derived from unresolved broad-band SED fitting to the resolved mass estimates: $m_{\text{resolved}} = m_{\text{unresolved}} / (-0.057 \log(\text{sSFR}) + 0.34)$, where sSFR is in units of yr^{-1} . We study the effect of varying spatial resolution by degrading the image resolution of the largest images and find a sharp decrease in the pixel-by-pixel mass estimate at a physical scale of approximately 3 kpc, which is comparable to spiral arm widths. The effects we observe are consistent with the ‘outshining’ idea which posits that the youngest stellar populations mask more massive, older – and thus fainter – stellar populations. Although the presence of strong dust lanes can also lead to a drastic difference between resolved and unresolved mass estimates (up to 45 per cent or 0.3 dex) for any individual galaxy, we found that resolving dust does not affect mass estimates on average. The strong correlation between mass discrepancy and sSFR is thus most likely due to the outshining systematic bias.

Key words: galaxies: statistics – galaxies: stellar content.

1 INTRODUCTION

Exactly how a galaxy’s stellar content evolves over time is unknown to us. In general, the build-up of stars – thought to be a steady stream of star formation (SF) complemented by stochastic bursts triggered by interactions with neighbouring galaxies – is halted at certain times by various quenching mechanisms, such as tidal stripping or feedback from e.g. active galactic nuclei. While the overall picture is clear, the precise star formation history (SFH) of any individual galaxy is hidden from us. Over the past decade, it has become apparent that a galaxy’s evolution is in large part described by its stellar mass. Several tight correlations have been found linking the stellar mass of a galaxy to a wide range of properties. A galaxy’s brightness and size (Trujillo et al. 2006; Williams et al. 2010),

rotational velocity or velocity dispersion (Faber & Jackson 1976; Tully & Fisher 1977), star formation rate (SFR; Reddy et al. 2006), if on the ‘main sequence’ (Daddi et al. 2007; Sawicki 2012b), metallicity (Savaglio et al. 2005; Mannucci et al. 2010), and mean stellar age (Gallazzi et al. 2005) are all well correlated with the mass of a galaxy’s stellar content.

Because a galaxy’s stellar mass plays such a vital role in our understanding of galaxy evolution, it behoves us to understand the estimating methods available as well as their limitations. Stellar population synthesis (SPS) modelling (Bruzual & Charlot 1993, 2003; Maraston 2005; Conroy, Gunn & White 2009; Conroy 2013, for a review) is a tool used nearly universally to estimate stellar masses in large surveys and at high redshift (e.g. Sawicki & Yee 1998; Kauffmann et al. 2003; Pérez-González et al. 2008; Marchesini et al. 2009; Ilbert et al. 2010; Sorba & Sawicki 2010; Maraston et al. 2013). At its most basic, an SPS model can be created by combining all the light from stellar models in a simple stellar population

* E-mail: rsorba@ap.smu.ca (RS); sawicki@ap.smu.ca (MS)

(SSP) – defined as a group of stars all born at the same time, with the same metallicity and with a mass distribution described by a chosen initial mass function (IMF) – and tracking how the combined light changes as the stars evolve with time. Composite stellar population models can then be created by adding different SSPs together as a function of time determined by some fiducial SFH. The stellar mass is determined by fitting an SPS model grid to observed broad-band photometry and scaling the stellar mass of the best-fitting model.

The uncertainties in the stellar mass estimate derived from broad-band SPS fitting can be large, up to a factor of 0.3 in dex when all uncertainties in model assumptions are taken into account (Conroy et al. 2009). This large variance does not, of course, account for any assumptions that we are not aware of. For example, Maraston et al. (2006) found that differing treatment of the thermally pulsating asymptotic giant branch stage of stellar evolution systematically decreased the predicted stellar mass of galaxies by a factor of 2. Note, however, that there is still some controversy over how to correctly treat these stars (Kriek et al. 2010). Another model assumption that systematically affects the derived stellar mass estimates is one’s choice of IMF, since the IMF directly affects the mass-to-light (M_*/L) ratio of the models. A third systematic bias was first noted by Sawicki & Yee (1998) and then emphasized by Papovich, Dickinson & Ferguson (2001) who stated that star-forming galaxies had the potential to hide underlying older stellar populations by outshining them. The fitting procedures preferentially favour matching the large amount of flux coming from the younger stellar population, and could potentially underestimate the M_*/L ratio by missing the relatively low amount of flux emanating from the older stars (where a majority of the stellar mass could rest). Unlike the two previously mentioned biases, the outshining bias is inherent to the broad-band SPS fitting procedure, rather than emerging explicitly from one’s choice of models. It is thus perhaps particularly insidious because it cannot be easily corrected for from one study to another. Moreover, because the bias would affect star-forming galaxies more strongly than quiescent galaxies, its differential nature could act to either produce spurious relations or mask true ones.

The outshining bias essentially arises from our lack of knowledge of the SFH of any particular galaxy and the SFH’s influence on the M_*/L ratio. If it were possible to know the precise SFH to use when creating a model spectral energy distribution (SED), then we would know the exact ratio of old to young stars and, hence, would not miss any of their mass when fitting preferentially to the flux emanating from the younger stellar population. However, since the SFH is unknown, its form must be assumed and often parametrized in the model grid to account for many possible differing histories. Maraston et al. (2010) and Pforr, Maraston & Tonini (2012) used mock galaxies to test the effects of mismatched SFHs on derived parameters, and found that the stellar masses of star-forming galaxies are typically underestimated, in part due to outshining, by 0.3 dex for $z \sim 2$ galaxies and up to 0.6 dex for lower redshift galaxies. They found that the mass measurement could be better reproduced by using an inverted- τ SFH (i.e. exponentially increasing), which is presumably closer to the true SFH of their galaxies. However, even if the true SFH is present in the model SED grid, unless it is the only SFH present, an outshining bias can still occur. Because the flux of younger stellar populations dominates so thoroughly at optical wavelengths, any two models with roughly similar young stellar components would have roughly an equal chance of being selected as the best-fitting model, even if one model had the true SFH and the other a vastly different one. Outshining can thus be regarded as the loss of constraints on the SFH (and thus M_*/L ratio) because the details are hidden behind bright, young stars. Gallazzi

& Bell (2009) explicitly examined the uncertainties in the M_*/L ratio in the case where the true SFH is present in the model library, with the assumption that the redshift is known and neglecting dust corrections. They were able to quantify biases from mismatched SFHs and in the prior distribution of SFHs compared to the true distribution, which they found could be as high as 0.1 dex.

The extent of any bias from outshining in our observations of low-redshift galaxies has been hinted at, but not rigorously determined. Drory, Bender & Hopp (2004) compared masses derived from spectra to photometric masses and found that for objects with strong $H\alpha$ equivalent widths (i.e. star-forming), the photometric mass was systematically lower than the spectroscopic mass by up to 0.15 dex. Zibetti, Charlot & Rix (2009) fit SPS models to individual pixels in nine Spitzer Infrared Nearby Galaxies Survey (SINGS) galaxies, and compared the resolved and unresolved mass estimates. They also found that the unresolved mass estimate (i.e. fitting all the light from the galaxy at once as if it were a point source) could be underestimated compared to the resolved mass by up to 40 per cent (0.15 dex). However, they attribute this effect to unresolved dust lanes, rather than star-forming regions. Taylor et al. (2010), on the other hand, compared stellar masses with dynamical masses and placed an upper limit on any differential bias in stellar mass estimates at less than 0.12 dex. It is clear that a systematic bias is present, although the large scatter in any individual mass measurement makes it difficult to put an exact value on the offset due to outshining. In order to have the best understanding of stellar mass estimates, it is crucial to better constrain this bias. The large statistical variance in stellar mass estimates necessitates the use of a large number of objects to penetrate through the noise.

With this in mind, we follow the approach of Zibetti et al. (2009) and compare spatially resolved versus unresolved mass estimates, as this method only requires broad-band photometry which is readily available from a myriad of different surveys. We set out to constrain the average systematic offset from fitting broad-band photometry of star-forming galaxies to SPS models. We stress that in this work we are in no way trying to determine the actual amount of stellar material in galaxies, but are instead focused on a comparative study between the pixel-by-pixel (PXP) and unresolved broad-band SED fitting mass estimates. We are solely interested in the effects of outshining as an inherent procedural bias. In Section 2 we describe our data and PXP SPS fitting procedure, and in Section 3 we discuss the resulting comparisons between resolved and unresolved stellar mass estimates. Throughout this work, we assume a *Wilkinson Microwave Anisotropy Probe 7* (Komatsu et al. 2011) flat Λ cold dark matter cosmology ($H_0 = 70.4 \text{ km s}^{-1} \text{ Mpc}^{-1}$, $\Omega_M = 0.272$) and use the AB magnitude system.

2 METHOD

2.1 Data

We used publicly available u , g , r , i , z data from the Sloan Digital Sky Survey (SDSS) Data Release 10 (Eisenstein et al. 2011) supplemented with publicly available NUV data from the *GALEX* Ultraviolet Atlas (GUA; Gil de Paz et al. 2007), which also provides measurements of the spectroscopic redshift, major and minor diameter, and morphological classification for each galaxy. Although FUV data were also available from *GALEX*, we found that their signal-to-noise ratio (S/N) was typically too low to get accurate photometry in a single pixel. These six bandpasses should provide more than adequate wavelength coverage to derive stellar masses from SPS fitting, which could be done using only the five SDSS

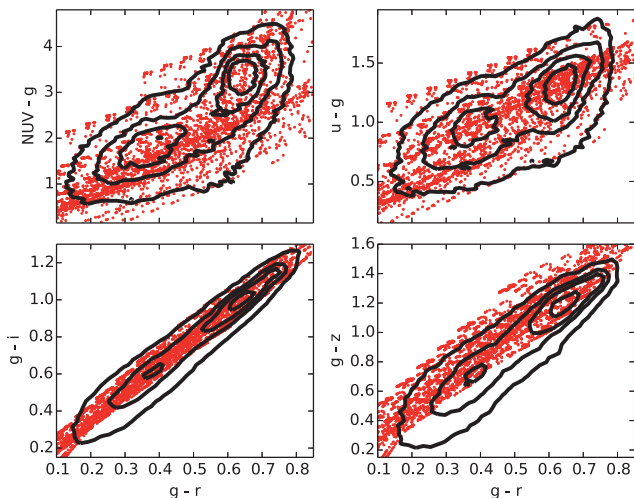


Figure 1. Colour–colour diagrams showing how our model colours compare with the observed photometry. The black lines represent the 10, 33, 66, and 90 per cent contour levels of the histogram of the brightest (*i*-band) quartile of pixels for all galaxies. The total number of pixels binned is 187 445. The red points are where our models lie in colour–colour space for a galaxy at $z = 0.0057$ which is the average redshift of our galaxy sample. The models generally show good agreement with the observations, tending to lie on the locus in each sub-plot.

filters¹ (e.g. Maraston et al. 2013). The NUV bandpass adds a second measurement below the 4000 Å break and provides additional information about the young stellar population and extinction. It acts to break some of the degeneracies inherent in the models (see Fig. 1).

Starting with the approximately 1000 objects in the GUA which contains all galaxies larger than 1 arcmin in diameter observed with *GALEX*, we cross-correlated with the SDSS frames using the bulk image search functionality of the Sloan website. We then visually inspected each matching frame and removed any galaxies that lay too close to the border of the SDSS frame. This step ensures that any edge effects, whether from the raw photometry or due to convolution (see below), will not affect a pixel’s final colours. Additionally, we removed any galaxies that spanned the entire SDSS frame since there would be no way to get an accurate background measurement for that frame. The remaining galaxies were processed following the procedure in Section 2.2, and colour images were made from the resulting aligned and point spread function (PSF) matched images. The colour images were again visually inspected and any galaxies with obvious artefacts (e.g. excessive bleeding from foreground stars) were discarded. In total, these criteria left us with 67 galaxies including eight elliptical, one lenticular, and four irregular galaxies, with the remainder being some form of spiral galaxy.

¹ We compared stellar mass estimates derived using only the five SDSS filters with those made with the additional NUV bandpass. We found that the inclusion of the NUV had a slight effect on mass estimates, increasing them by approximately 7 per cent on average, although with large scatter. However, this average difference was present in both the resolved and unresolved mass estimates, and so does not qualitatively affect our conclusions. We postulate that the observed mass difference arises from the NUV limiting the amount of unrealistic extinction available to the fit. That is to say, we found that the pixels (and galaxies) were nearly universally fitted with higher extinction models when the NUV data were not included. The greater amount of extinction for the same amount of flux led to greater mass estimates when the NUV data were not included.

2.2 Processing

For each galaxy, we downloaded the appropriate SDSS frame, mask, and PSF which was read at the centre of the galaxy using the `READ_PSF` software package provided on the SDSS website.² The *GALEX* raw count, high-resolution relative response, and flag images were downloaded. We use the *GALEX* PSF available on the *GALEX* website.³ We created a square cut-out of the *GALEX* images centred on the galaxy with sides equal to 1.5 times the galaxy’s major diameter. Although background-subtracted intensity images are provided, we found through visual inspection of the sky background images that the provided background maps tended to overestimate the background of extended galaxies, likely due to diffuse radiation from the galaxy (see also Zou et al. 2011). We thus derived our own background estimates in the raw count cut-out by first masking the galaxy and then performing a sigma-clipping function in 50 pixel by 50 pixel square regions and fitting a plane to the background estimates in each region. Since counts from NUV photons are few, the estimated background value in each step of the sigma-clipping algorithm was set to be equal to the variance (rather than the mean) of the values in each square region. This was done to account for the lack of symmetry in the Poisson distribution when number counts are low; using the mean would overestimate the background value slightly. A background-subtracted intensity map with units of counts per second per pixel was created using the formula

$$I = (C - B)/R, \quad (1)$$

where C represents the raw count map, B the background map, and R the relative response. We then created a root-mean-square (rms) noise map for the intensity image by

$$\sigma_I = \sqrt{\sigma_C^2 + \sigma_B^2}/R, \quad (2)$$

where σ_C is the square root of the count image (i.e. Poissonian uncertainty) and σ_B is the standard deviation of the background determined using our sigma-clipping method above.

The SDSS images are already background subtracted as part of the SDSS pipeline, but this process overestimates the background of extended objects (Blanton et al. 2005; Bernardi et al. 2007). We therefore reinstated the background subtracted by the SDSS pipeline and performed our own background estimation, similar to what is described above, but using the mean in each square region as the best background estimate as allowed by the much larger count numbers. Each SDSS frame had to be converted to data numbers using the provided calibration layer of the FITS file. The rms images were then made for the SDSS images using the formula

$$\sigma_I = \sqrt{x\sigma_C^2 + x\sigma_B^2}, \quad (3)$$

where I is now in units of nanomaggies, B is again the background map, x is the calibration layer value, and σ_C , the uncertainty in the data number image, is now given by

$$\sigma_C = \sqrt{C/g + \sigma_{\text{dark}}^2} \quad (4)$$

with C/g the data number divided by the gain to yield the Poissonian variance of the counts and σ_{dark} is the Poissonian noise from the dark current.

Having created background-subtracted images with corresponding noise maps in each of the desired bandpasses, we next aligned

² https://www.sdss3.org/dr10/algorithms/read_psf.php

³ <http://www.galex.caltech.edu/researcher/techdoc-ch5.html>

the SDSS images with the *GALEX* cut-out and resampled the SDSS pixel scale to the *GALEX* pixel scale ($1.5 \text{ arcsec pixel}^{-1}$) using the *SWARP* software package (Bertin et al. 2002). Although losing spatial resolution seems contrary to our purpose, the reasons for degrading the SDSS pixel scale are threefold. (1) Artificially chopping up an NUV pixel into smaller pixels may not result in realistic spatial distribution of the NUV photons (even if interpolation is used), which would lead to erroneous colours in each individual pixel. (2) Combining the SDSS pixels together leads to a higher S/N which is crucial when striving for accurate photometry on a PXP basis. (3) Having fewer pixels speeds up computation time of all future steps immensely.

We also performed a re-alignment and resampling of the SDSS PSF by placing the PSF at the same location in the frame as the centre of the galaxy and using the same parameters for *SWARP*. It is important to have an estimate of the PSF prior to resampling, otherwise one is likely to have an undersampled PSF and encounter problems when trying to estimate it from the resampled image.

The *GALEX* PSF was the broadest, so to ensure that each pixel contains light from the same physical location it was necessary to find a convolution kernel that would translate each image from its current PSF to the broadest PSF. We found the transformation kernel by taking the ratio of the two PSFs in Fourier space and then inverse-transforming the result. We masked any saturated pixels and foreground stars (found using the 2MASS catalogue; Skrutskie et al. 2006) and then convolved each SDSS image with the appropriate transformation kernel using *SCIPY*'s `ndimage convolve` routine with pixel values set to zero outside the image. The uncertainty was propagated by convolving the variance map with the square of the transformation kernel to yield the variance map of the convolved SDSS image.

With the resulting set of background-subtracted, aligned, resampled, PSF-matched images, we then made photometry catalogues of each pixel with an S/N of at least 5 in every SDSS filter. To make a fair comparison between PXP SED fitting result and those using spatially unresolved fluxes, we calculated the unresolved magnitudes not from aperture photometry, but by summing the flux from each pixel included in the PXP catalogue and then converting to AB magnitude. Doing this is key as it ensures that the same amount of light is being compared in each case.

2.3 Models

We fit the broad-band photometry from the six SDSS and *GALEX* bandpasses to model SEDs created using the *FSPS* population synthesis code (Conroy et al. 2009; Conroy & Gunn 2010). Our model set is comprised of two-component burst models similar to those used in Noll et al. (2009) where there is an underlying older stellar population combined with a more recent burst of SF. In principle, each of the two components (young and old) can have its own SFH, age (i.e. the time since the burst was initiated), IMF, and metallicity history, as well as various parameters controlling how dust absorbs and re-emits light. Here, we describe our chosen model parameters, which we found to adequately represent our photometric observations (listed in Table 1).

We parametrized the SFH of the older stellar component as a delayed (sometimes referred to as extended) exponential decay (i.e. of the form $\psi(t) \sim te^{-t/\tau}$ so that SF at first increases linearly with time) with e-folding time τ_{old} spaced roughly logarithmically between 0.1 and 10. The delayed- τ models (Lee et al. 2010) are a good compromise between the commonly used τ models and the inverted- τ models of Maraston et al. (2010), particularly for low-

Table 1. Parameters used in two-component model SEDs.

Symbol	Value(s)
Z_{old}	0.0016 ($\sim 0.084 Z_{\odot}$)
Z_{young}	0.019 (Z_{\odot})
τ_{old}	[0.1, 0.25, 0.625, 1.25, 2.5, 5, 10]
τ_{young}	0.1
t_{old}	10
t_{young}	[6, 6.5, 7, 7.5, 7.75, 8, 8.25, 8.5, 8.75, 9, 9.25, 9.5]
f_{young}	[0, 10^{-4} , 10^{-3} , 0.01, 0.1, 0.25, 0.5, 0.75, 0.9, 0.99]
$E(B - V)$	[0, 0.05, 0.1, 0.15, 0.2, 0.25, 0.3, 0.35, 0.4, 0.5]

The ages are in units of log years.

redshift galaxies which have seen a decline in SFR density since $z \sim 2$ (Madau et al. 1996; Sawicki, Lin & Yee 1997). Simha et al. (2014) found that delayed- τ models were much more successful at reproducing the SFH of simulated galaxies than plain τ models. The SFH of the younger burst is a standard exponential decay with τ_{young} held constant at 0.1. Each of the young and old components also has an age (t). For the older component, this was held constant with SF starting 10 billion years ago, while the younger burst had onset ages ranging from 10^9 to 10^6 yr ago. We combined the older and younger components so that the mass fraction of the younger component has a value f_{young} which we allowed to vary between 0 and 1. The two-component models used here provide a wide variety of SFHs and are similar in construction to those of Noll et al. (2009) which were found to adequately represent galaxies in the SINGS survey similar to those being studied here.

We used a Chabrier (2003) IMF for all models and set the metallicity of the younger component equal to solar metallicity and that of the older component equal to 0.0016 (i.e. ~ 8 per cent Z_{\odot}). The choice of significantly sub-solar metallicity for the older stellar component was motivated by the simplistic assumption that the overall metallicity of the Universe should be lower at earlier times, as well as the results of Zou et al. (2011), which showed evidence for a double-peaked metallicity distribution in NGC 628 with the metal-poor component peaking at $[\text{Fe}/\text{H}] = -1.15$. Additionally we found that the inclusion of a sub-solar metallicity component yielded a model space that better matched the observed PXP colours (see Fig. 1). Particularly, the $g - z$ colour was too red if solar metallicity was used in both stellar components.

For extinction due to dust, we assumed a Calzetti et al. (2000) dust law with $E(B - V)$ values ranging between 0 and 0.5. To save computation time and limit the parameter space, we arbitrarily enforced models comprised mainly of older stars to only have $E(B - V)$ values less than 0.3.

In total, our parameter space is defined by four free parameters: τ_{old} , t_{young} , f_{young} , and $E(B - V)$. In Fig. 1, we show a comparison between our models at $z = 0.0057$ (the average redshift of our galaxy set) and the PXP photometry for the brightest i -band quartile of pixels histogrammed from all galaxies. Although there is a larger spread in the observations than the models due to photometric noise and differing redshifts, our models appear to generally lie on the locus of the observations and adequately span the colour space. It is important to note, however, that since we are doing a comparative study of resolved versus unresolved fitting, it is not imperative that our choice of models actually represent reality to the fullest extent as long as the same set of models is used throughout the study.

In order to determine the best-fitting model to a given galaxy's pixel's broad-band photometry, we redshifted the model spectrum to the spectroscopic redshift of the galaxy and corrected for dust in the Milky Way (Schlegel, Finkbeiner & Davis 1998; Schlafly &

Finkbeiner 2011). The spectrum was then convolved with the broad-band filter transmission curves to give model magnitudes in each of the six bandpasses of interest. We used the SEDFIT software package (Sawicki 2012a) to generate the model magnitudes and then to find the best-fitting model employing a χ^2 minimization routine. In order to determine uncertainties, SEDFIT performs a number of iterations for each pixel with the photometry randomly perturbed by selecting a random variable from a Gaussian distribution with standard deviation equal to the uncertainty in the photometry. We performed 300 iterations and used the median mass of these iterations as our final mass estimate. This avoids biases in the χ^2 best-fitting estimate (see, e.g., Taylor et al. 2011).

3 RESULTS

In Fig. 2, we show false colour images and best-fitting model property maps for a subset of our galaxies (the full set is available as an online supplement). The false colour images are made using u -, g -, and i -band images as the blue, green, and red colours, respectively. The property maps show the strength of the D4000 break as a proxy for stellar age (since two-component models do not have a well-defined age; see e.g. Noll et al. 2009), the stellar mass, the SFR, and the extinction spatial distributions in each galaxy. As expected, regions in the spiral arms that are very bright in the u band (i.e. flux generated from younger stars) are fitted to models with weaker D4000 breaks and SFRs that are higher than the surrounding population. The mass distribution, however, is relatively smooth, emphasizing that the M_*/L ratio in each pixel is a function of the stellar population, and that older stars comprise the bulk of a galaxy's total stellar mass while not contributing as significantly to the galaxy's total brightness.

3.1 Unresolved fitting can underestimate stellar mass

In order to determine how well-unresolved broad-band SED fitting can recover the true stellar mass content of a galaxy, we calculated the ratio of the unresolved stellar mass to the 'true' stellar mass (here assumed to be the sum of the stellar mass of the best-fitting model in each pixel). We plot this ratio as a function of unresolved specific star formation rate (sSFR, SFR per unit stellar mass) in Fig. 3. We calculated the average unresolved-to-resolved mass ratio for different morphologies in each of the 300 Monte Carlo iterations and show the median and 1σ spread as horizontal lines in blue for spiral galaxies and red for elliptical and lenticular galaxies. Doing so reveals that the stellar mass estimates of elliptical/lenticular galaxies (red squares) tend to have stellar mass estimates that are roughly the same whether resolved or unresolved. On the other hand, spiral galaxies (blue circles) are typically underestimated by 13 per cent (0.06 dex) on average when structure is unresolved. Moreover, there is a clear decline in the unresolved-to-resolved mass ratio for the spiral galaxies as sSFR increases. To parametrize this dual nature, we fit the broken linear relation

$$f(x) = \begin{cases} b_1 & : x \leq p \\ b_2 + (b_1 - b_2)x/p & : x > p \end{cases} \quad (5)$$

(which is a horizontal line with intercept b_1 up to some point $x = p$ and has some other slope thereafter) to the galaxies in each of the 300 Monte Carlo iterations. The median and 1σ confidence intervals of these fits are shown as the purple solid line and shaded region in Fig. 3. In all Monte Carlo instances, there is a clear trend of increasing average mass discrepancy with increasing sSFR, with unresolved stellar mass estimates underestimated by 25 per cent (0.12

dex) at the highest sSFRs in our set of galaxies. Put another way, to correct the unresolved stellar mass estimate to the PXP stellar mass estimate for these high sSFRs, one would have to add 33 per cent to the unresolved mass, which is much more significant than adding the statistical average correction of 15 per cent (0.06 dex).

Since the break points of the piecewise functions all exist at the lowest extremes of our measured sSFRs, separating the data into two regimes may be an unnecessary complication. For simplicity, we fit a simple linear relation to our median Monte Carlo mass ratios (shown as the purple dashed line in Fig. 3). This line lies within the shaded 1σ confidence region, and provides a close approximation to the more complex median of the piecewise fit distribution. It also allows for a simple formula to convert an unresolved stellar mass estimate to PXP one based on the unresolved sSFR. The conversion relation is

$$m_{\text{resolved}} = \frac{m_{\text{unresolved}}}{-0.057 \log(\text{sSFR}) + 0.34}, \quad (6)$$

where sSFR is in units of yr^{-1} .

3.2 Origin of the discrepancy

In Fig. 4, we superimpose false colour images of each of the galaxies on to their location in Fig. 3. It is apparent that the most egregious outliers from the one-to-one relation (NGC 3190, NGC 4419, and NGC 5719 located in the lower-left corner with unresolved-to-resolved mass ratios less than 0.65, but also edge-on M98 near the top centre) all have strong dust lanes with heavy amounts of extinction running through them. To try to determine whether resolving dust or SFR is the dominant driver of the unresolved-to-resolved mass discrepancy, we refitted the PXP photometry but constrained the extinction to be the same as determined from the best fit to the unresolved photometry. The results are shown in Fig. 5 where we plot the ratio between the fixed extinction PXP mass and the free extinction PXP mass versus sSFR. In this figure, the closer the points lie to the same mass ratio as in Fig. 3, the more important role dust plays in the unresolved-to-resolved mass discrepancy, whereas points near the one-to-one line are little affected by resolving dust. In the cases of NGC 3190, NGC 4419, and NGC 5719, the effects of resolving the strong dust lanes account for the majority of the difference between unresolved and resolved stellar mass estimates, as they again lie well below the one-to-one relation. We also find that the large majority of the spread in elliptical galaxies and those with low sSFR are due to allowing extinction to be a free parameter from pixel to pixel. Removing this freedom essentially eliminates any difference between resolved and unresolved stellar mass estimates for the low-sSFR galaxies.

What is not present in Fig. 5 is any trend with sSFR. Even though the mass difference due to resolving dust can be drastic for any one galaxy, the deviation appears centred on the one-to-one line so that, on average, not resolving dust does not systematically bias mass estimates of large numbers of galaxies. The strong linear trend seen in Fig. 3 must then be due to distinguishing the strongly and weakly star-forming regions and, thus, accounting for the outshining bias in broad-band SED fitting.

3.3 The effect of varying spatial resolution

In an effort to understand how resolution affects the PXP parameter estimations, we artificially degraded the images of the 10 largest face-on spiral galaxies by progressively doubling the pixel scale. This process was done for those 10 (of our 67) galaxies with large

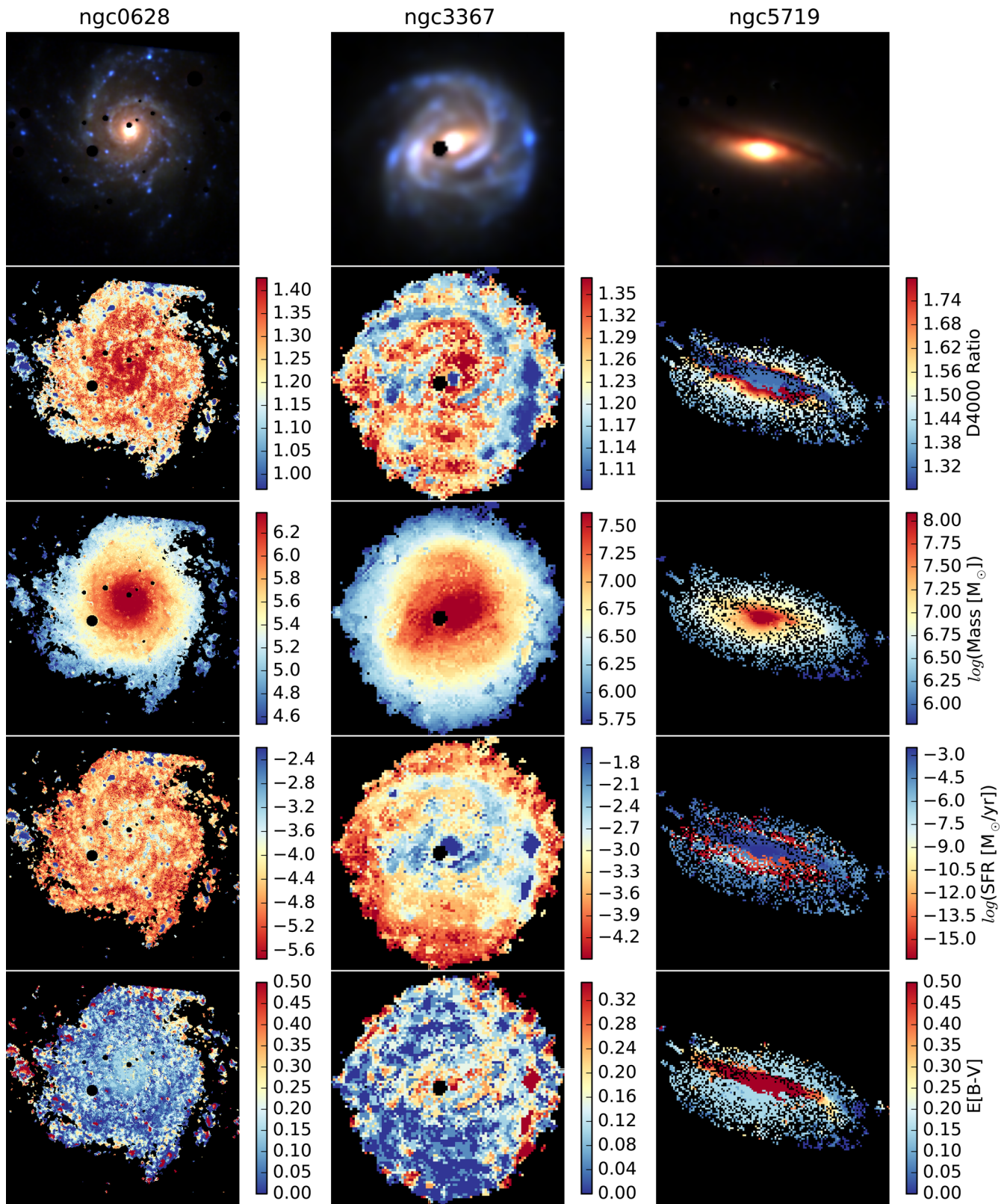


Figure 2. Maps showing (from top to bottom) false colour *ugi*, 4000 Å break strength, stellar mass, SFR, and extinction in each pixel for three illustrative galaxies from our sample of 67. Areas of low S/N as well as those containing foreground Galactic stars are masked out in black. Maps for the remaining galaxies can be found in an online supplement.

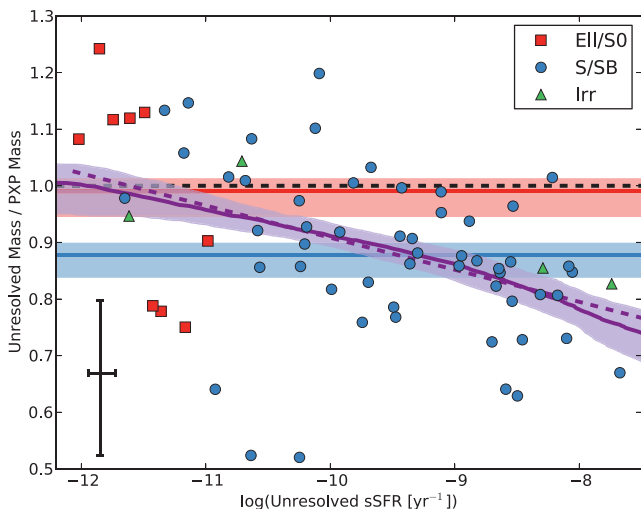


Figure 3. Ratio of unresolved stellar mass estimate to the PXP stellar mass estimate as a function of sSFR. The dashed horizontal black line represents a one-to-one correspondence. Spiral galaxies (blue points) tend to lie below the one-to-one line, while elliptical galaxies (red points) tend to lie on it (on average). The blue line shows the average ratio of the spiral galaxies indicating that ≈ 13 per cent of the stellar mass is missed by fitting all the light as if the galaxy were an unresolved point source. The red line shows the average ratio for elliptical galaxies, which lies nearly on the one-to-one ratio. The shaded blue and red regions show the 1σ confidence regions for these average ratios as determined from Monte Carlo iterations. The purple solid line and shaded region show the median and 1σ confidence region of fitting a broken linear relationship to all the galaxies in each of the 300 Monte Carlo iterations. The purple dashed line shows a linear fit to the data. A clear trend with sSFR is present. Typical error bars are shown in the lower-left corner.

enough areas that after eight degradation steps they were completely unresolved and contained within one or two pixels. Fig. 6 shows quartile ranges for the ratio of the degraded resolution PXP stellar mass estimate over the full-resolution PXP stellar mass estimate as a function of physical scale. At the highest resolutions, the mass ratio slowly decreases to about 0.97, but drops sharply when the pixel scale becomes greater than $2\text{--}3 \text{ kpc pixel}^{-1}$. The mass ratio then stabilizes near the 13 per cent underestimate mark, although with much higher variance in the quartile ranges. It should be made clear that any one galaxy does not display a mass ratio that monotonically decreases with increasing resolution; the variance of mass estimates from SED is too large to show this. It is only by looking at an ensemble of galaxies that we can see on average how the mass estimate behaves as the spatial resolution gets poorer and poorer.

The physical scale of 3 kpc per resolution element (here being pixel because the artificial degradation makes each pixel larger than the PSF) corresponding to the comparatively steep drop in mass ratio is much larger than the size of typical star-forming regions in these galaxies (a few hundred parsecs; Efremov 1995; Gusev, Egorov & Sakhibov 2013). The scale may be more commensurate with the width of spiral arms (Kennicutt & Hodge 1982; Seigar & James 1998). To adequately separate young and old stellar populations and thus minimize the effect of outshining bias, it seems necessary to at least be able to resolve any spiral structure in the galaxy. This result may just be an artefact of our resolution study sample however, as these galaxies all have star-forming populations concentrated in spiral arms. Note also that several irregular galaxies shown in Fig. 4 follow the linear trend due to outshining despite the lack of any clear spiral structure. Nevertheless, as spiral structure has

been observed to have formed much earlier in the history of the Universe than previously thought possible (Law et al. 2012), it is still relevant to know that resolving spiral arms goes a long way towards mitigating any bias due to outshining. Perhaps more generally, one can say that PXP SED fitting can greatly reduce the effects of outshining only when any structure that distinguishes older and younger stellar populations is able to be resolved. In the case of our low-redshift sample, this structure is spiral arms with a physical scale of approximately 3 kpc. If this level of resolution is impossible, one can use the conversion relation given in Section 3.1.

4 DISCUSSION

4.1 Testing model space dependence

As discussed in Gallazzi & Bell (2009), the model template grid used constitutes a prior assumption which can bias the M_*/L ratios determined from broad-band colours. In order to test the extent to which our results depend on our model space, we performed two tests. First, Gallazzi & Bell (2009) found that including a large fraction of bursty models could underestimate the M_*/L ratio of older, smooth-SFH galaxies. Although we found that the unresolved and PXP masses of ellipticals do not differ on average, we nevertheless tested the robustness of our results using a smooth SFH. While it is impossible to exhaustively test every SFH, we repeated our procedure using τ SFH models and arrived at qualitatively similar results (namely the unresolved mass estimates of galaxies with low sSFRs were no different from the resolved mass estimates on average, whereas star-forming galaxies were underestimated by approximately 0.07 dex on average, although without as strong a dependence on sSFR). From this we conclude that, while our results are not entirely independent of our choice of SFH (one could always construct unrealistic SFHs that would produce vastly different results, say if all star-forming models had no underlying older stellar population at all), for any reasonable or commonly adopted SFH, our results should be qualitatively similar, with unresolved stellar mass estimates of star-forming galaxies underestimated by somewhere between 0.05 and 0.08 dex on average.

Secondly, as examined in Gallazzi & Bell (2009), the S/N of the observations combined with the model template prior distribution can lead to biased results. In brief, they found that when the model template set is a mixture of bursty and smooth SFHs with differing M_*/L ratios, good data will constrain the fits to only those models with the proper M_*/L ratio. But, as the amount of noise in the data increases, the fit will be more free to explore the model space, and hence the determined M_*/L ratio will depend on the ratio of bursty to smooth SFHs in the model template set. Since our stated criterion for a pixel to be included in our mass estimation was S/N greater than 5 in all SDSS bandpasses, this effect could play a prominent role in our results. However, in practice the S/N in g, r, i is much better than that in either u or z , and our criterion is essentially equivalent to $S_u/N_u > 5$ (although, in a very small percentage of pixels, the z band is the limiting one). The large S/N in g, r, i give the fits much less freedom than initially implied by our selection criteria. To test this, we took the unresolved photometry (which has extremely good S/N) and artificially increased the uncertainty in each bandpass, refitting the median Monte Carlo mass at each step. To realistically approximate the uncertainty growth in each bandpass for our data, for each galaxy we created histograms of the S/N in each bandpass and found the i th percentile where i is a multiple of 10. We converted this to an uncertainty in magnitude for the Monte Carlo fits. Fig. 7 shows the ratio of the increasingly noisy mass

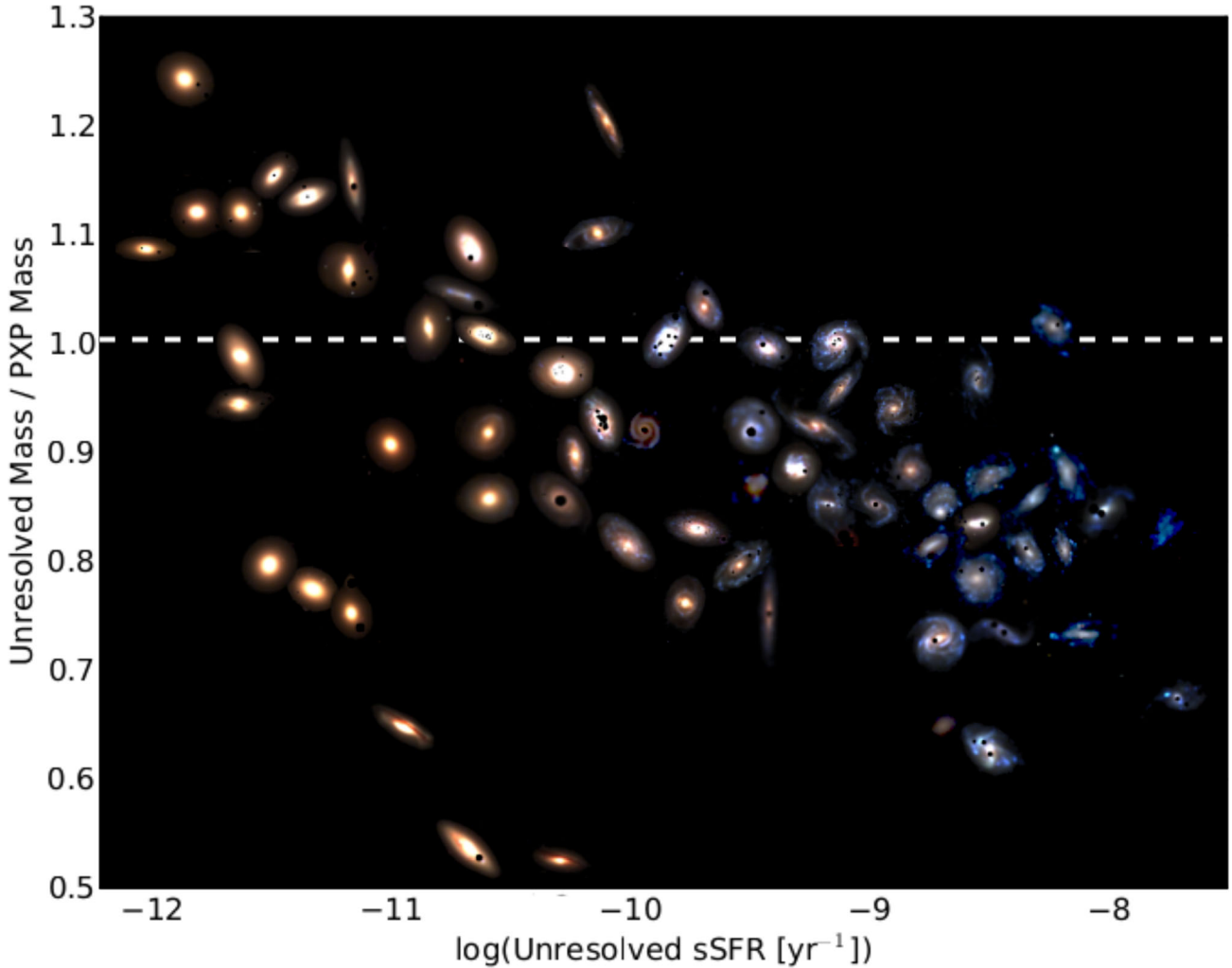


Figure 4. Same as Fig. 3, except showing a false colour *ugi* image for each galaxy. All galaxies have been scaled to be roughly the same size, and some of their positions have been slightly altered for clarity.

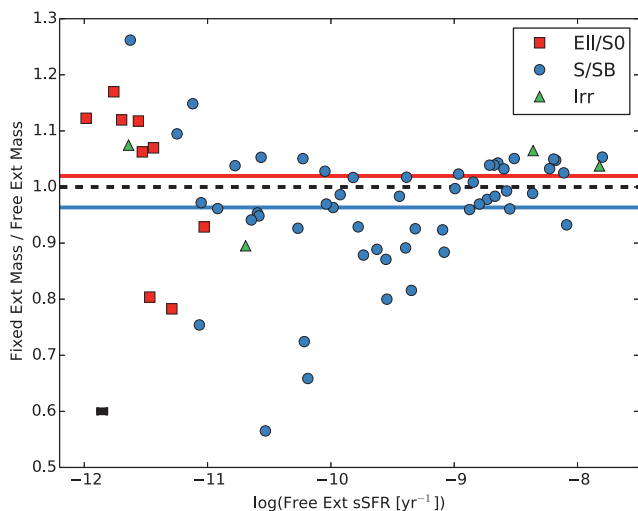


Figure 5. As in Fig. 3, a mass ratio is plotted versus the sSFR. Blue circles are morphologically classified as spirals, red squares ellipticals, and green triangles irregular galaxies. Here, the vertical axis shows the ratio of the PXP mass found when holding the extinction value fixed to the amount determined by the best-fitting unresolved estimate to the PXP mass found when extinction is a free parameter.

estimate to the unresolved mass estimate as a function of *u*-band S/N. The typical *r*-band S/N at this stage is also shown for reference, and is typically 8–10 times that of the *u* band. The binned average (red squares) shows little deviation from a one-to-one correspondence. There may be a slight downward trend at $S/N_u < 10$, but it is at the 2 percent level. Since the low-S/N pixels are also the least massive, any bias of this level in their mass determination has a net effect of much less than 1 percent on the total PXP mass of the galaxy. Additionally, since the noisy mass would underestimate the true mass, this bias would only work to increase the unresolved-to-resolved mass discrepancy found above, if only very slightly.

4.2 Impact on previously derived relations

The average offset of 13 per cent for star-forming galaxies is equivalent to approximately 0.06 dex. This is not an outstandingly large discrepancy, and any current relationship with stellar mass would not change dramatically if corrected for this offset. However, the differential nature of the offset (affecting higher sSFR galaxies more than those with lower sSFR) can compound the effect given the right circumstances. For instance, plotted in Fig. 8 in green is the star-forming main sequence (SFR– M_* relation) from Whitaker

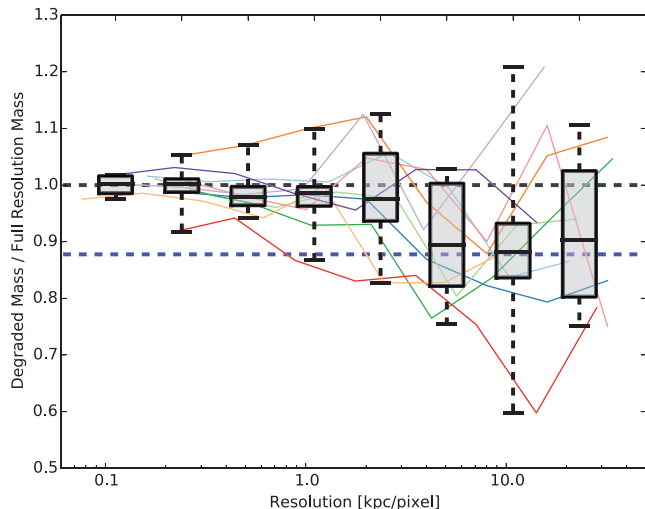


Figure 6. Ratio of degraded resolution PXP stellar mass estimate to the highest resolution PXP stellar mass at various pixel scales for 10 spiral galaxies with the largest area. The boxes and whiskers represent quartiles of the data grouped in bins of width ~ 0.33 dex in resolution. As in Fig. 3, the dashed black line shows the one-to-one correspondence and the dashed blue line the average mass ratio for spiral galaxies. There is a sharp transition in the mass ratio near 3 kpc pixel^{-1} . The thin solid coloured lines show the individual tracks for each of the 10 galaxies.

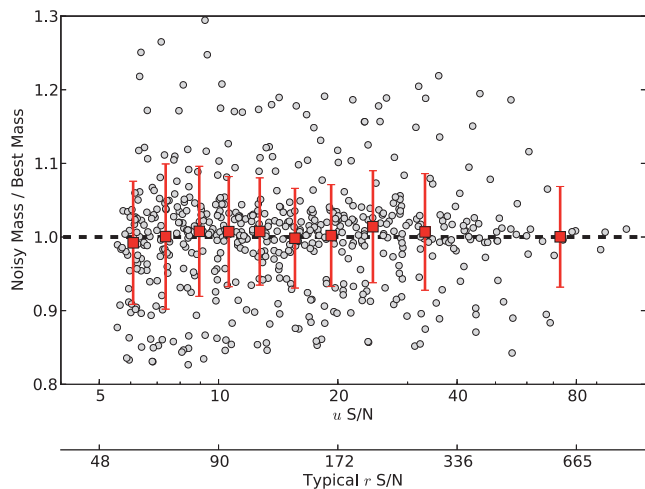


Figure 7. Ratio of mass estimates from unresolved photometry with artificially increased uncertainties to those with lowest uncertainties as a function of u -band S/N. The artificially increased uncertainty in each bandpass is determined by taking the i th percentile of the S/N histogram where i is a multiple of 10. The typical r -band S/N determined from these percentiles is also shown for reference. The grey points show the mass ratio for each galaxy at each noise percentile. The red squares show the average of the grey points in bins of 1/10th of the data. The black dashed line shows the one-to-one correspondence. The mass estimates show no bias with increasing S/N within our cut-off limit of 5.

et al. (2012) and isometallicities of the M_* - Z -SFR surface from Mannucci et al. (2010) in blue. Dashed red lines show corrections to these relations based on interpolating the purple line in Fig. 3 of this work. The shallow slope of the Whitaker et al. (2012) relation in the SFR- M_* log-log plane leads to little difference when corrected for outshining. At best one can say that the slope is a little steeper, requiring slightly faster evolution from the flatter relation at higher redshift (assuming no effect of outshining at higher redshift). How-

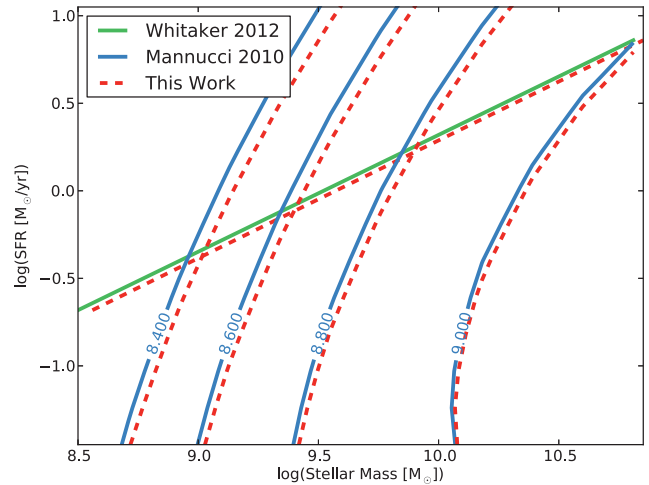


Figure 8. SFR- M_* relation from Whitaker et al. (2012) in green and isometallicity contours of the M_* - Z -SFR relation from Mannucci et al. (2010) in blue. The numbers on the contours are in units of $12 + \log(\text{O}/\text{H})$. The red dashed lines show corrections to these relations based on this work.

ever, the effects of outshining become more apparent when metallicity dependence is included in the relationship. The M_* - Z -SFR relationship exists throughout the SFR- M_* log-log plane, allowing one to see the larger offsets in high-sSFR regions (upper left of Fig. 8) compared to lower sSFR regions. The steeper slope of the isometallicities also leads to outshining corrections being larger in the full M_* - Z -SFR (though still not extremely large).

The sSFR dependence of the unresolved-to-resolved mass difference can manifest itself in other, possibly less obvious ways. For instance, Patton et al. (2013) compare SFRs in interacting galaxy pairs with a control sample selected to have similar masses as the paired galaxies. Since the SFR is enhanced in the paired galaxies, however, so too is the sSFR. Thus, a larger correction must be applied to the paired galaxy's unresolved mass estimate than must be applied to the control sample, possibly making the control sample not representative. It turns out not to be an issue in this particular case, because the maximum SFR enhancement is approximately a factor of 2, meaning the difference between the enhanced corrected mass and control corrected mass is only 5 per cent, well within their stated control bounds of 0.1 dex in stellar mass. However, awareness that mass selected samples may not be as homogeneous in mass due to differing sSFRs is still important to acknowledge.

Even within a single galaxy the sSFR-dependent mass correction may be important to note. Several works (e.g. Allen et al. 2006; Simard et al. 2011; Mendel et al. 2014) decompose a galaxy into inner and outer components (i.e. bulge and disc) with SF occurring primarily in the outer regions. The sSFR of the outer region is thus enhanced compared to the inner region, and so a differential correction (perhaps up to 0.1 dex) must be applied when comparing the masses of the inner and outer components. In general, the outshining mass correction should be considered for broad-band SED fitting in any cases with high sSFRs, or when comparing two sets of data with differing sSFRs.

4.3 Outshining at higher redshifts

How the systematic bias described above might change with redshift is an open question. The sSFR of star-forming galaxies increases with redshift (Feulner et al. 2005), and so we might expect the outshining effect to become more drastic at earlier times in the

Universe. For example, taken at face value, the relation given by the purple line in Fig. 3 implies that galaxies with sSFRs between -8 and -7 yr^{-1} (rates much more common during the era of peak SFR density) would have to be corrected by between 0.1 and 0.2 dex, respectively. However, as outshining is a product of incorrect SFHs, galaxies at higher redshift should be less affected because there has been less time for differences in the assumed versus true SFH to accumulate. Put another way, there would be fewer older stars (and hence less mass) hiding behind the bright younger stars simply because there has not been enough time to form a significant older stellar population. See, for example, Pforr et al. (2012) on the effects of assumed SFH as a function of redshift. It is clear that, at some value of redshift, outshining would cease to be an issue as there would not be a significant older population of stars to obscure. In the limiting case, the first burst of stars formed in a galaxy would essentially be an SSP, and thus have no outshining.

PXP SED fitting has been performed for high-redshift galaxies at $z \sim 1$ and $z \sim 2$ by Wuyts et al. (2012) using data taken with Wide Field Camera 3 on board the *Hubble Space Telescope* (*HST*) as part of the Cosmic Assembly Near-infrared Deep Extragalactic Legacy Survey (CANDELS; Grogin et al. 2011; Koekemoer et al. 2011). They found that the unresolved mass estimate from these galaxies was robust, and that there was no discrepancy between the resolved and unresolved mass estimates. Their PSF-matched images had a resolution of 0.18 arcsec FWHM (full width at half-maximum), which corresponds to a physical scale of 1.46 and 1.54 kpc at redshifts 1 and 2, respectively. From our results in Section 3.3 (Fig. 6), this resolution should be adequate to detect any discrepancy if it existed at high redshift. However, Wuyts et al. (2012) also further bin pixels to increase S/N, making their effective resolving power much worse the PSF FWHM. Indeed, they state that they do find a mass discrepancy of 0.2 dex for $z \sim 2$ star-forming galaxies when no pixel binning is performed, although they attribute this to low-S/N pixels having spurious M_*/L ratios. How outshining affects mass estimates at high redshift thus remains an open question, one that may not be able to be answered until the advent of the next generation of telescopes such as the *James Webb Space Telescope* or Thirty Meter Telescope, which will provide roughly 2.5 and 10 times greater resolution than the *HST*, respectively.

5 CONCLUSIONS

We fit SPS models to broad-band fluxes in each pixel for 67 nearby galaxies and compared the stellar mass estimates found from summing each pixel's median Monte Carlo mass with the median Monte Carlo mass found when the models were fitted to all the light from the galaxy at once, as if it were an unresolved point source.

The unresolved mass estimate systematically underestimated the resolved mass estimate, displaying a clear trend of increasing discrepancy with increasing sSFR. Galaxies with low sSFR ($\log(\text{sSFR}[\text{yr}^{-1}]) \sim -12$) were consistent with no mass discrepancy between resolved and unresolved mass estimates, whereas unresolved mass estimates of the highest sSFR galaxies ($\log(\text{sSFR}[\text{yr}^{-1}]) \sim -8$) typically underestimate the mass by 25 per cent (0.12 dex). We provide a conversion formula (equation 6) to correct unresolved mass estimates at low redshift based on a galaxy's sSFR.

We found the mass discrepancy's correlation with sSFR to be due to outshining, i.e. young stellar populations obscuring older stellar populations behind their bright flux. However, several egregious outliers from this relation were caused by the presence of strong dust lanes. The presence of dust can cause differences between the

resolved and unresolved mass estimates of up to 45 per cent (0.35 dex). Although very significant for individual galaxies, resolving the 2D distribution of dust did not have any effect on average stellar mass estimates.

By artificially degrading the resolution of the largest spiral galaxies, we found that a resolution of at least 3 kpc is needed to significantly reduce the systematic underestimation in stellar mass due to outshining. This scale is commensurate with the width of spiral arms in these galaxies.

Although it is unclear how the relation between resolved and unresolved stellar mass estimates changes at higher redshifts, we recommend that caution be taken when considering mass estimates of galaxies with high sSFRs that have been derived from broad-band SED fitting. Be aware that these masses are likely systematically underestimated by 13–25 per cent (0.06–0.12 dex) on average due to outshining. The differential nature of this effect should be taken into account when comparing masses of populations with different sSFRs (e.g. disc versus bulge, 'mass-matched' galaxies with a range of SFRs). In the case of any individual galaxy, note that the presence of dust lanes can greatly impact the mass estimate (Changing something by a factor of 2 changes dex by 0.3.), but that the effects from dust should average out when considering an ensemble.

ACKNOWLEDGEMENTS

We thank the anonymous referee for many insightful comments that greatly improved the quality of this paper. We are very grateful to Tiffany Fields for her help with the images presented in this work, and thanks are due to Anneya Golob and Liz Arcila-Osejo for useful discussions and a careful reading of the manuscript.

This work was supported financially by the Natural Sciences and Engineering Research Council (NSERC) of Canada, including an NSERC Graduate Scholarship to RS and an NSERC Discovery Grant to MS.

Computational facilities are provided by ACENet, the regional high performance computing consortium for universities in Atlantic Canada. ACENet is funded by the Canada Foundation for Innovation (CFI), the Atlantic Canada Opportunities Agency (ACOA), and the provinces of Newfoundland and Labrador, Nova Scotia, and New Brunswick.

This research made use of *ASTROPY*, a community-developed core *PYTHON* package for Astronomy (Robitaille et al. 2013), as well as many of the routines available in the *SCIPY* and *NUMPY* software packages.

Some of the data presented in this paper were obtained from the Mikulski Archive for Space Telescopes (MAST). STScI is operated by the Association of Universities for Research in Astronomy, Inc., under NASA contract NAS5-26555. Support for MAST for non-HST data is provided by the NASA Office of Space Science via grant NNX13AC07G and by other grants and contracts.

Funding for SDSS-III has been provided by the Alfred P. Sloan Foundation, the Participating Institutions, the National Science Foundation, and the US Department of Energy Office of Science. The SDSS-III website is <http://www.sdss3.org/>. SDSS-III is managed by the Astrophysical Research Consortium for the Participating Institutions of the SDSS-III Collaboration including the University of Arizona, the Brazilian Participation Group, Brookhaven National Laboratory, Carnegie Mellon University, University of Florida, the French Participation Group, the German Participation Group, Harvard University, the Instituto de Astrofísica de Canarias, the Michigan State/Notre Dame/JINA Participation Group, Johns Hopkins University, Lawrence Berkeley National Laboratory, Max

Planck Institute for Astrophysics, Max Planck Institute for Extraterrestrial Physics, New Mexico State University, New York University, Ohio State University, Pennsylvania State University, University of Portsmouth, Princeton University, the Spanish Participation Group, University of Tokyo, University of Utah, Vanderbilt University, University of Virginia, University of Washington, and Yale University.

REFERENCES

- Allen P. D., Driver S. P., Graham A. W., Cameron E., Liske J., de Propris R., 2006, *MNRAS*, 371, 2
- Bernardi M., Hyde J. B., Sheth R. K., Miller C. J., Nichol R. C., 2007, *AJ*, 133, 1741
- Bertin E., Mellier Y., Radovich M., Missonnier G., Didelon P., Morin B., 2002, in Bohlender D. A., Durand D., Handley T. H., eds, *ASP Conf. Ser. Vol. 281, Astronomical Data Analysis Software and Systems XI*. Astron. Soc. Pac., San Francisco, p. 228
- Blanton M. R. et al., 2005, *AJ*, 129, 2562
- Bruzual G., Charlot S., 1993, *ApJ*, 405, 538
- Bruzual G., Charlot S., 2003, *MNRAS*, 344, 1000
- Calzetti D., Armus L., Bohlin R. C., Kinney A. L., Koornneef J., Storchi Bergmann T., 2000, *ApJ*, 533, 682
- Chabrier G., 2003, *PASP*, 115, 763
- Conroy C., 2013, *ARA&A*, 51, 393
- Conroy C., Gunn J. E., 2010, *ApJ*, 712, 833
- Conroy C., Gunn J. E., White M., 2009, *ApJ*, 699, 486
- Daddi E. et al., 2007, *ApJ*, 670, 156
- Drory N., Bender R., Hopp U., 2004, *ApJ*, 616, L103
- Efremov Y. N., 1995, *AJ*, 110, 2757
- Eisenstein D. J. et al., 2011, *AJ*, 142, 72
- Faber S. M., Jackson R. E., 1976, *ApJ*, 204, 668
- Feulner G., Gabasch A., Salvato M., Drory N., Hopp U., Bender R., 2005, *ApJ*, 633, L9
- Gallazzi A., Bell E. F., 2009, *ApJ*, 185, 253
- Gallazzi A., Charlot S., Brinchmann J., White S. D. M., Tremonti C. A., 2005, *MNRAS*, 362, 41
- Gil de Paz A. et al., 2007, *ApJS*, 173, 185
- Grogin N. A. et al., 2011, *ApJ*, 197, 35
- Gusev A. S., Egorov O. V., Sakhibov F., 2013, *MNRAS*, 437, 1337
- Ilbert O. et al., 2010, *ApJ*, 709, 644
- Kauffmann G. et al., 2003, *MNRAS*, 341, 33
- Kennicutt R. J., Hodge P., 1982, *ApJ*, 253, 101
- Koekemoer A. M. et al., 2011, *ApJ*, 197, 36
- Komatsu E. et al., 2011, *ApJS*, 192, 18
- Kriek M. et al., 2010, *ApJ*, 722, L64
- Law D. R., Shapley A. E., Steidel C. C., Reddy N. A., Christensen C. R., Erb D. K., 2012, *Nature*, 487, 338
- Lee S.-K., Ferguson H. C., Somerville R. S., Wiklind T., Giavalisco M., 2010, *ApJ*, 725, 1644
- Madau P., Ferguson H. C., Dickinson M. E., Giavalisco M., Steidel C. C., Fruchter A., 1996, *MNRAS*, 283, 1388
- Mannucci F., Cresci G., Maiolino R., Marconi A., Gnerucci A., 2010, *MNRAS*, 408, 2115
- Maraston C., 2005, *MNRAS*, 362, 799
- Maraston C., Daddi E., Renzini A., Cimatti A., Dickinson M., Papovich C., Pasquali A., Pirzkal N., 2006, *ApJ*, 652, 85
- Maraston C., Pforr J., Renzini A., Daddi E., Dickinson M., Cimatti A., Tonini C., 2010, *MNRAS*, 407, 830

- Maraston C. et al., 2013, *MNRAS*, 435, 2764
- Marchesini D., van Dokkum P. G., Förster Schreiber N. M., Franx M., Labbé I., Wuyts S., 2009, *ApJ*, 701, 1765
- Mendel J. T., Simard L., Palmer M., Ellison S. L., Patton D. R., 2014, *APJS*, 210, 3
- Noll S., Burgarella D., Giovannoli E., Buat V., Marcellac D., Muñoz Mateos J. C., 2009, *A&A*, 507, 1793
- Papovich C., Dickinson M., Ferguson H. C., 2001, *ApJ*, 559, 620
- Patton D. R., Torrey P., Ellison S. L., Mendel J. T., Scudder J. M., 2013, *MNRAS*, 433, L59
- Pérez-González P. G. et al., 2008, *ApJ*, 675, 234
- Pforr J., Maraston C., Tonini C., 2012, *MNRAS*, 422, 3285
- Reddy N. A., Steidel C. C., Fadda D., Yan L., Pettini M., Shapley A. E., Erb D. K., Adelberger K. L., 2006, *ApJ*, 644, 792
- Robitaille T. P. et al., 2013, *A&A*, 558, A33
- Savaglio S. et al., 2005, *ApJ*, 635, 260
- Sawicki M., 2012a, *PASP*, 124, 1208
- Sawicki M., 2012b, *MNRAS*, 421, 2187
- Sawicki M., Yee H. K. C., 1998, *AJ*, 115, 1329
- Sawicki M. J., Lin H., Yee H. K. C., 1997, *AJ*, 113, 1
- Schlafly E. F., Finkbeiner D. P., 2011, *ApJ*, 737, 103
- Schlegel D. J., Finkbeiner D. P., Davis M., 1998, *ApJ*, 500, 525
- Seigar M. S., James P. A., 1998, *MNRAS*, 299, 685
- Simard L., Mendel J. T., Patton D. R., Ellison S. L., McConnachie A. W., 2011, *APJS*, 196, 11
- Simha V., Weinberg D. H., Conroy C., Dave R., Fardal M., Katz N., Oppenheimer B. D., 2014, preprint ([arXiv:e-prints](https://arxiv.org/abs/1408.0001))
- Skrutskie M. F. et al., 2006, *AJ*, 131, 1163
- Sorba R., Sawicki M., 2010, *ApJ*, 721, 1056
- Taylor E. N., Franx M., Brinchmann J., van der Wel A., van Dokkum P. G., 2010, *ApJ*, 722, 1
- Taylor E. N. et al., 2011, *MNRAS*, 418, 1587
- Trujillo I. et al., 2006, *ApJ*, 650, 18
- Tully R. B., Fisher J. R., 1977, *A&A*, 54, 661
- Whitaker K. E., van Dokkum P. G., Brammer G., Franx M., 2012, *ApJ*, 754, L29
- Williams R. J., Quadri R. F., Franx M., van Dokkum P., Toft S., Kriek M., Labbé I., 2010, *ApJ*, 713, 738
- Wuyts S. et al., 2012, *ApJ*, 753, 114
- Zibetti S., Charlot S., Rix H. W., 2009, *MNRAS*, 400, 1181
- Zou H. et al., 2011, *AJ*, 142, 16

SUPPORTING INFORMATION

Additional Supporting Information may be found in the online version of this paper:

(<http://mnras.oxfordjournals.org/lookup/suppl/doi:10.1093/mnras/stv1235/-/DC1>).

Please note: Oxford University Press are not responsible for the content or functionality of any supporting materials supplied by the authors. Any queries (other than missing material) should be directed to the corresponding author for the paper.

This paper has been typeset from a $\text{\TeX}/\text{\LaTeX}$ file prepared by the author.